ACS Photonics

pubs.acs.org/journal/apchd5 Article

Observation of Negative Effective Thermal Diffusion in Gold Films

Alexander Block,[¶] Renwen Yu,[¶] Ieng-Wai Un,[¶] Sebin Varghese, Matz Liebel, Niek F. van Hulst, Shanhui Fan, Klaas-Jan Tielrooij, and Yonatan Sivan*

Cite This: *ACS Photonics* 2023, 10, 1150−1158 Read Online

ACCESS | Metrics & More | Article Recommendations

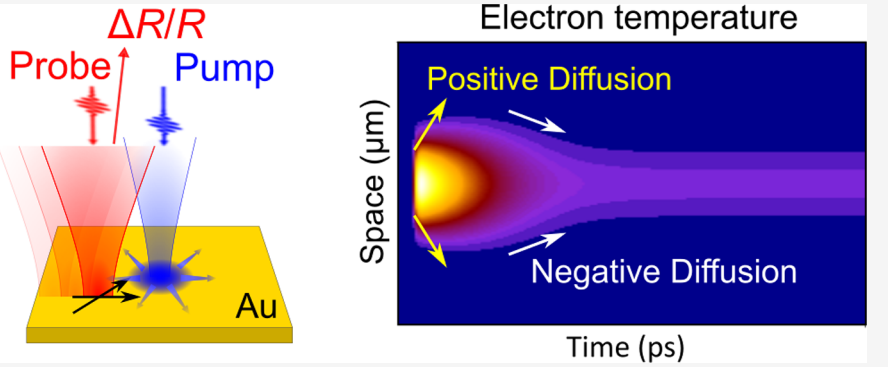

ABSTRACT: Ultrafast light-induced spatiotemporal dynamics in metals in the form of electron and/or phonon heating is a fundamental physical process that has tremendous practical relevance. In particular, understanding the resulting lateral heat transport is of key importance for various (opto)electronic applications and thermal management but has attracted little attention. Here, by using scanning ultrafast thermo-modulation microscopy to track the spatiotemporal electron diffusion in thin gold films, we show that a few picoseconds after the optical pump there is unexpected heat flow from phonons to electrons, accompanied by negative effective thermal diffusion, characterized by shrinking of the spatial region with increased temperature. Peculiarly, this occurs on the intermediate time scale, between the few picosecond long thermalization stage and the many picosecond stage dominated by thermoacoustic vibrations. We accurately reproduced these experimental results by calculating the spatiotemporal photothermal response based on the two-temperature model and an improvement of the standard permittivity model for gold. Our findings facilitate the design of nanoscale thermal management strategies in photonic, optoelectronic, and high-frequency electronic devices.

KEYWORDS: *plasmonics, energy transport, heat generation and diffusion, high-resolution microscopy, permittivity modeling*

INTRODUCTION

Heat dynamics and transport mediated by optically excited charge carriers in conductors is a fundamental aspect of nanosystems which also plays an essential role in many advanced applications.[1] Indeed, it has proven useful for photodetection,[2−6] nanoscale imaging,[7,8] data storage,[9] thermal emission,[10,11] photocatalysis,[12−14] heat management,[15] etc. In the quest of improving the speed of optoelectronic devices, ultrafast optical heating induced by laser pulse absorption also serves as a method of great practical interests.[16−19]

Ultrafast pump−probe techniques are widely used to study the ultrafast carrier and heat transport in metals and semiconductors under optical excitation.[20] These studies indicated that, in metals, the absorbed optical energy from the pump is first deposited into the electron subsystem, driving it away from thermal equilibrium. Femtosecond scale electron−electron (e−e) collisions during the sub-picosecond transient lead to the gradual re-emergence of a thermal distribution yet at an elevated electron temperature. The lattice remains almost thermally undisturbed in this initial femtosecond time period. At sub-picosecond to picosecond times, the effect of electron−phonon interactions becomes more pronounced,[21] causing a transfer of some of the electron heat to the phonon subsystem; this results in electron cooling and phonon heating. At a few tens to hundreds of picoseconds, the metal undergoes thermally induced acoustic oscillations,[22−24] and finally, the system reaches thermal equilibrium via heat transfer to the environment. Similar heat dynamics occur in low electron density Drude metals,[25] as well as graphene and other 2D (semi)metals, albeit with shorter time scales: thermalization within the electron system occurs within tens

Received: December 8, 2022
Published: March 28, 2023

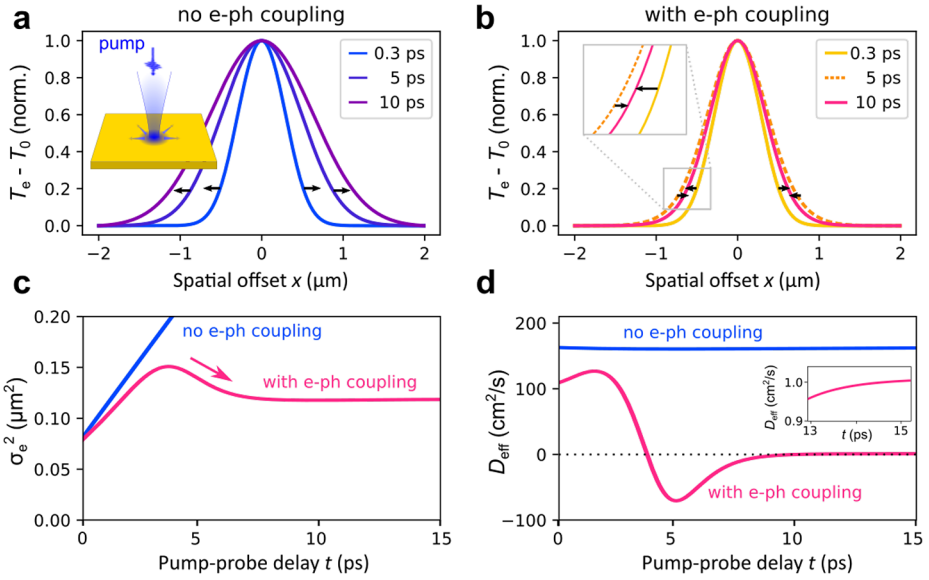

Figure 1. Spatiotemporal dynamics of the electron temperature. (a) Electrons are excited locally by an ultrafast laser pulse (pulse duration t_p = 200 fs), as shown in the inset. We present the calculated spatial profiles of the normalized electron temperature distribution $(T_e - T_0)/\max\{T_e - T_0\}$, with the profile width denoted by σ_e, at different pump−probe delay times (see labels), where T_0 = 300 K is the ambient temperature. The spatial profiles are calculated without considering electron−phonon coupling. Black arrows indicate the temporal dynamics of the spatial profiles. (b) Same as panel (a) but including the electron−phonon interaction. The inset shows a zoomed view for better visibility of the dynamics. (c) Temporal evolution of σ_e^2 fitted from the spatial profiles shown in panels (a) and (b) for cases with (magenta curve) and without (blue curve) electron−phonon coupling. (d) Temporal evolution of the effective thermal diffusivity D_{eff} extracted from σ_e^2 shown in panel (c) for cases with (magenta curve) and without (blue curve) electron−phonon coupling. The inset shows the later time scales when the effective diffusion converges at around 1 cm^2/s.

of femtoseconds, followed by electron−phonon-induced cooling on a picosecond time scale.[26]

However, although the experimental techniques properly resolved the temporal dynamics, they usually provided little information about spatial dynamics. Indeed, direct real-space mapping to observe the carrier diffusion in both space and time has remained challenging. Only recently, the combination of ultrafast spectroscopy and nanoimaging techniques, such as electron microscopy, near-field microscopy, as well as ultrafast pump−probe and photocurrent microscopy, has opened up new avenues to visualize microscopic transport.[27−33] Specifically, in refs 30, 31, 34 and 35, it was shown that the subpicosecond stages of the in-plane spatiotemporal heat dynamics in thin noble metal films are dominated by electron diffusion, whereas beyond 10 ps, the diffusion slows down as it is then dominated by the phonons. The intermediate time scale of 5−10 ps showed a rather noisy transition between these two stages, exposing a clear lack of understanding of the intermediate regime between these two stages of electron-dominated transport and phonon-dominated transport. Several theoretical works discussed diffusion in metals, including the intermediate regime,[36−40] yet they lack experimental validation.

In this work, we focus on the heat dynamics in the intermediate regime. We report on a counterintuitive phenomenon of (transient) negative diffusion of the electron heat in a thin gold film, caused by the localized cooling of electrons below the local phonon temperature. We start with a thorough analysis of this phenomenon and argue that apparent negative diffusion can occur whenever two coupled systems are characterized by distinct populations with dissimilar diffusivities. Indeed, apparent negative diffusion has recently been observed in bright/dark excitonic[41] and singlet/triplet[42] systems. We adopt the two-temperature model (TTM)[43,44] which has been widely used to predict the electron and phonon temperature distributions in metals pumped by ultrashort laser pulses. We monitor the spatial distribution of the electron temperature T_e undergoing an effective thermal diffusion at a rate D_{eff}. We also demonstrate theoretically the emergence of a negative effective diffusion, whereby the spatial profile of the electron temperature distribution in thin gold films transiently shrinks in space. We then study experimentally the picosecond-scale effective diffusion via ultrafast thermomodulation microscopy[30] in a thin film of Au, where a near-IR pulse (∼805 nm central wavelength) probes the temperature-dependent transient reflectivity ($\Delta R/R$) as a function of both pump−probe time delay and pump−probe spatial offset. We show that due to greater sensitivity of the Au permittivity to the phonon temperature, the shrinking of the electron temperature spot size does not leave a clear signature on the reflectivity spot dynamics $\Delta R/R$. In order to expose the effect, we replaced the near IR probe by a visible probe (∼620 nm central wavelength). Unlike the near-IR probe, this probe induces also efficient interband transitions. These are shown, using an improvement of the conventional model for the contribution of these transitions to the metal permittivity, to induce a relatively greater sensitivity of the permittivity to the electron temperature. Accordingly, the spatiotemporal dynamics of the reflectivity becomes more similar to that of the electron temperature, thus making it clearly observed in the measurements. Our theory closely matches the experimental data and thus demonstrates the occurrence of transient negative diffusion in one of the most common and representative (3D) material systems, namely, a thin metal film.

https://doi.org/10.1021/acsphotonics.2c01916
ACS Photonics 2023, 10, 1150−1158

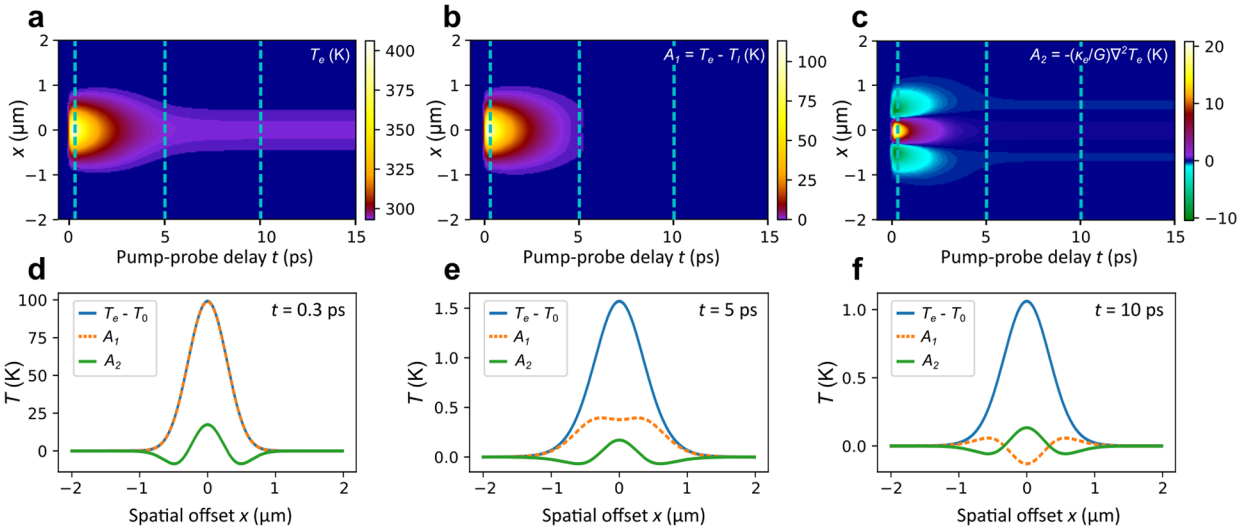

Figure 2. Analysis for the spatiotemporal dynamics of the electron temperature. (a–c) Contour plots for the spatiotemporal dynamics of the following three quantities: T_e, $A_1 = T_e - T_l$, and $A_2 = (\kappa_e/G)\nabla^2 T_e$. (d–f) Spatial profiles of those three quantities at three selected delay times: 0.3, 5, and 10 ps, indicated by vertical dashed lines shown in panels (a–c).

RESULTS

We consider laser-induced electron temperature dynamics (see inset of Figure 1a), where an ultrafast laser pulse (pulse duration t_p = 200 fs, pump fluence is 10 μJ/cm^2 causing a maximal electron temperature of ~400 K) with a Gaussian profile (profile width, defined as its standard deviation, σ_p = 0.3 μm) impinges onto a thin gold film to create high-temperature electrons. In this work, we focus on the temperature dynamics that follows the sub-picosecond-scale thermalization of the electron system. Accordingly, we can safely ignore the nonthermal stage of the dynamics.

For the hypothetical case of no electron–phonon coupling, the spatiotemporal dynamics of the electron subsystem's temperature is subjected to a heat diffusion equation

$$C_e \frac{\partial T_e}{\partial t} = \nabla\cdot(\kappa_e \nabla T_e) + S(\mathbf{r}, t) \quad (1)$$

where C_e and κ_e are the heat capacity and thermal conductivity of the gold electron and S is the source term representing the absorbed optical energy from the pump pulse (see refs 30 and 45–47 for more details). Here, we are interested in the lateral (in-plane) heat diffusion and consider metal films thin enough (~50 nm) for which it was verified numerically that the temperature distribution is homogeneous across the film thickness.

Within this simple model, the temporal dynamics of the squared width σ_e^2, for the in-plane spatial distribution of T_e, are governed by $\partial\sigma_e^2/\partial t = 2D(t)$ with $D(t) = \kappa_e/C_e$ being the instantaneous diffusion coefficient.[48] As a result, we find that the spatial profiles of the electron temperature expand in space as time evolves, as shown in Figure 1a, where the pump pulse arrives at t = 0 (with initial ambient temperature T_0 = 300 K). The spreading character of the spatial profile indicates a positive $D(t)$.

A more realistic model would also include electron–phonon coupling. This plays an important role in the spatiotemporal dynamics of T_e, which is reflected in the TTM[43,44]

$$C_e \frac{\partial T_e}{\partial t} = \nabla\cdot(\kappa_e \nabla T_e) - G(T_e - T_l) + S(\mathbf{r}, t) \quad (2)$$

$$C_l \frac{\partial T_l}{\partial t} = \nabla\cdot(\kappa_l \nabla T_l) + G(T_e - T_l) \quad (3)$$

where C_l and κ_l are the heat capacity and thermal conductivity of the gold lattice and G is the electron–phonon coupling coefficient (see refs 30 and 45–47). After taking into account the electron–phonon coupling, the spatial profiles of the electron temperature shrink when comparing their shapes at two subsequent time instances t = 5 and 10 ps despite an expansion at earlier times, as shown in Figure 1b. The time evolution of σ_e^2 extracted from Figure 1a,b is shown in Figure 1c. Surprisingly, we find a decreasing σ_e^2 starting from $t \approx 3$ ps (magenta curve) when the electron–phonon interaction affects the electron temperature dynamics, in stark contrast to the situation without considering the electron–phonon coupling where σ_e^2 increases linearly with time (blue curve). Moreover, one can define and extract an effective instantaneous diffusion coefficient for the electron temperature as $D_{eff}(t) = 0.5\ \partial\sigma_e^2/\partial t$ from Figure 1c. The extracted D_{eff} with electron–phonon coupling considered (magenta curve) is displayed in Figure 1d, and a negative D_{eff} is indeed observed from $t \approx 3$ ps to 10 ps. This is in stark contrast to the constant positive diffusion coefficient when excluding electron–phonon coupling (blue curve). At later times, our model recovers to the state of positive D_{eff}. Essentially, the diffusion coefficient converges to be $(\kappa_e + \kappa_l)/(C_e + C_l)$, i.e., the well-known equilibrium thermal diffusivity around 1 cm^2/s, as shown in the inset of Figure 1d, which leads to a slow increase of σ_e^2, as shown in Figure 1c.

In order to understand the mechanism underlying the observed negative diffusion, we present the spatiotemporal dynamics of T_e, $A_1 = T_e - T_l$, and $A_2 = -(\kappa_e/G)\nabla^2 T_e$ in Figure 2a–c, respectively. A_1 and A_2 represent the influence of the electron–phonon coupling and electronic heat diffusion, respectively, on the electron temperature dynamics. They enable one to compare directly the temperature difference term to the magnitude and evolution of the diffusion term. In more detail, $A_1 > 0$ (or $A_2 > 0$) means that the corresponding process should result in a decrease of the local electron temperature with time and vice versa, as seen from eq 2. At the early stages of the dynamics (t = 0.3 ps, Figure 2d), we have $A_1 > 0$ (orange curve) over the whole spatial extent of the heat

https://doi.org/10.1021/acsphotonics.2c01916
ACS Photonics 2023, 10, 1150–1158

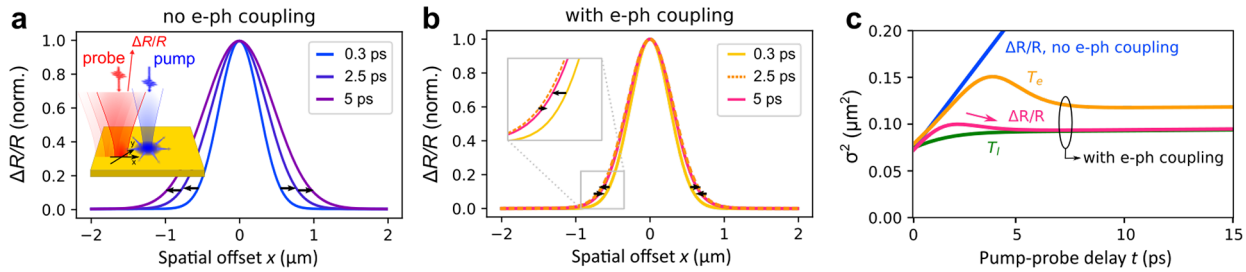

Figure 3. Spatiotemporal dynamics of transient reflection signal $\Delta R/R$. (a) Probe pulse is used to monitor the local electron temperature distribution by measuring the spatiotemporal dynamics of the temperature-dependent transient reflectivity $\Delta R/R$, as shown in the inset. We present the calculated spatial profiles of the normalized $\Delta R/R$ at different delay times. The spatial profiles are calculated without considering the electron−phonon coupling. Black arrows indicate the temporal dynamics of the spatial profiles. (b) Same as panel (a) but including the electron−phonon interaction. The inset shows a zoomed-in view for better visibility of the dynamics. (c) Temporal evolution of the squared width σ_R^2 fitted from the spatial profiles shown in panels (a) and (b) for cases with (magenta curve) and without (blue curve) electron−phonon coupling. We also show temporal evolution of σ^2 for both electron T_e (orange curve) and lattice T_l (green curve) temperatures with electron−phonon coupling as a reference.

spot, which means that electrons tend to dissipate heat to the lattice everywhere within the gold film right after the optical pump. In particular, the most efficient heat dissipation to the lattice occurs at the center ($x = 0$). On the other hand, we have $A_2 > 0$ at the center, but $A_2 < 0$ away from the center (green curve). In other words, the electronic heat flows away from the center which broadens the spatial profile at early times.

At the intermediate stages of the dynamics ($t = 5$ ps, Figure 2e), the shape of the spatial distribution of A_2 (green curve) is similar to the case for $t = 0.3$ ps, and the electronic heat diffusion remains outward from the center. We still have $A_1 > 0$ everywhere; however, its shape has drastically changed (orange curve). Noticeably, the maximum of A_1 is no longer at the center, which means that electrons dissipate heat more quickly at locations away from the center. This fact leads to an instantaneous shrinking of the spatial profile of T_e and a negative effective thermal diffusion coefficient. Finally, at the later stages of the dynamics ($t = 10$ ps, Figure 2f), a quasi-equilibrium is established between electron and lattice subsystems. As a result, from Figure 2b, one can see that $T_e \approx T_l$ over the whole spatial extent at $t = 10$ ps. Interestingly, we have $A_1 < 0$ (i.e., $T_e < T_l$) at the center (orange curve), and A_1 counterbalances A_2 (green curve), leading to a quasi-steady-state with a small thermal diffusion coefficient D_{eff}.

To observe the ultrafast spatiotemporal dynamics of charge carriers, we utilize a spatially resolved pump−probe technique, where an optical probe is scanned across the sample surface in order to measure the temperature-dependent transient differential reflection signal $\Delta R(\epsilon(T_e,T_l))/R(\epsilon(T_e,T_l))$ locally (see the inset of Figure 3a and the Methods section). This approach yields spatiotemporal dynamics of $\Delta R/R$, as an indirect measure of the electron and lattice temperatures, as shown in Figure 3. Without considering the electron−phonon coupling, the spatial profiles of $\Delta R/R$ expand with time, as shown in Figure 3a, which is similar to the observations in Figure 1a. After accounting for the electron−phonon coupling, we find again the shrinking in the spatial profiles between two time instances $t = 2.5$ and 5 ps, as shown in Figure 3b. Note that the temperature dependence in $\Delta R/R$ resides in the temperature-dependent gold permittivity $\epsilon(T_e,T_l)$[30,49−51] (see the Methods section for more details), which causes a much weaker shrinking effect compared with the results shown in Figure 1b. We compare the time evolution of the squared width σ^2 extracted from the spatial profiles of $\Delta R/R$ (magenta curve, now named σ_R^2) with those from T_e (orange curve, σ_e^2) and T_l (green curve) in Figure 3c, where σ_R^2 slowly starts decreasing starting from $t \approx 2.5$ ps. In addition, the shrinking of σ_R^2 occurs earlier than that of σ_e^2 due to the nontrivial temperature dependence in $\Delta R/R$. As a reference, a linear increase of σ_R^2 with time is found (blue curve) when ignoring the electron−phonon interaction.

In the experiment (see Methods), we image the light-induced spatiotemporal dynamics of a 50 nm thin gold film by performing pump−probe measurements where we control the spatial offset between pump and probe pulses, in addition to the usual control of temporal delay. We excite the sample with a pump fluence of ∼0.3 mJ/cm^2. By spatially scanning the probe beam relative to the stationary, tightly focused pump spot, we recorded the transient reflectivity $\Delta R/R$ profiles at different pump−probe time-delays, from 0 to 20 ps. Our spatial accuracy is determined by the signal-to-noise ratio and is estimated at ∼20 nm. The measured time evolution of σ_R^2 of a Gaussian fit is shown in Figure 4 for two different probe wavelengths. In both cases, we observe an initial fast broadening of the spatial profiles (0−3 ps), followed by a much slower broadening at longer time-delays. For the shorter probe wavelength, we also observe a substantial decrease in σ_R^2

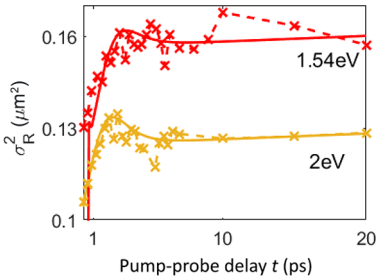

Figure 4. Gaussian width of the differential reflectivity spot as measured (crosses) and compared to the theoretical prediction (solid lines) for probe wavelengths of (2 eV, orange) and (1.54 eV, red). The error (67% confidence interval) is around ±0.006 μm^2, such that the theory−experiment agreement is satisfactory. While the trend of the experimental data for the 1.54 eV probe wavelength is inconclusive, a clear refocusing stage can be identified for the shorter wavelength. We have offset the calculation results by 50 nm (100 nm) for the 1.54 eV (2 eV) probe wavelength, which could be related to some very fast initial hot carrier diffusion that is not captured in the model.

https://doi.org/10.1021/acsphotonics.2c01916
ACS Photonics 2023, 10, 1150−1158

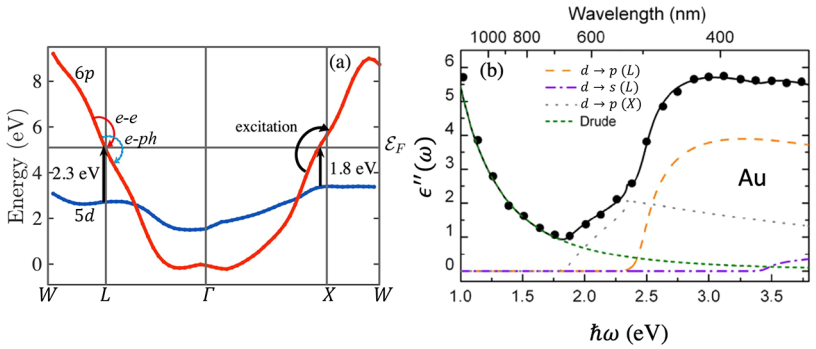

Figure 5. (a) Schematic of Au band structure adapted from ref 58. Red and blue lines correspond to the 6p and 5d bands, respectively. Fermi level is denoted by horizontal line $\mathcal{E}_F$ at $\mathcal{E} \approx 5$ eV, and the gap between 5d and the Fermi level is around 1.8 and 2.3 eV near X and L points, respectively. (b) Imaginary part of the dielectric constant for Au: Dots are experimental data. Green dashed line, orange dashed line, purple dot-dashed line, and gray dotted lines are Drude, d → p at L point, p → s at L point, and d → p at X point, respectively. The black solid line corresponds to the total dielectric constant, ϵ_{tot}. Adapted with permission from ref 20. Copyright 2014 Springer Nature.

in this transition regime, indicating negative diffusion, in agreement with our calculations; see Figure 4.

CONCLUSIONS

In conclusion, we have shown that the spatiotemporal electron temperature dynamics in gold films can result in unexpected negative thermal diffusion, i.e., a shrinking of the spatial profiles of the electron temperature, after ultrafast optical excitation. Based on the two-temperature model providing temporal and spatially resolved electron temperature dynamics, we first theoretically attribute this effect to the intrinsic electron−phonon interaction in gold. We then experimentally demonstrate this effect by tracking optically induced thermal diffusion in a thin gold film in time and space with femtosecond and nanometer resolution using ultrafast thermo-modulation microscopy. The measured dynamics agree well with the theoretical predictions as well as with the recent results of refs 31 and 52. In ref 31, the TTM parameter space was investigated, while the negative diffusion effect was less pronounced due to the NIR probe wavelength (similar to that in ref 30), and in ref 52, a more pronounced effect was achieved by varying the fluence and sample thickness via a simpler model that considers two diffusive, yet uncoupled temperature profiles (see also ref 48, Ch. 3.2.3).

Our results obtained in a simple metallic film show that the apparent negative diffusion that was recently observed in arguably more exotic material systems, with exciton[41] and singlet/triplet[42] diffusion, is a more general phenomenon. The effect occurs whenever there are two diffusing species that are coupled and have dissimilar diffusivities. In ref 41, these were bright and dark excitons in 2D layered transition metal dichalcogenides; in ref 42, these were singlet and triplet states in organic semiconductors; and in the present case these were electrons and phonons in a metal film. Our findings should motivate further investigations into the complex spatiotemporal heat dynamics occurring at the intermediate time range of a few picoseconds.

METHODS

Fabrication and Pump−Probe Measurement. We fabricated the sample by the thermal evaporation of 50 nm of gold onto a cleaned glass coverslip. We use an experimental setup as described in ref 53. In brief, a mode-locked laser (repetition frequency f_{rep} = 80 MHz) generates pulses centered at 1030 nm. Most of the laser output power is used to pump an optical parametric oscillator (OPO) which has a tunable signal output between 1320 and 2000 nm. To obtain the pump pulse for the measurement (with a wavelength of 515 nm), we used a lithium triborate (LBO) crystal to generate the second harmonic of the fundamental laser source. The probe beam centered at a wavelength of 805 nm (620 nm) is obtained from the second (third) harmonic of the signal output of the OPO. We combine the pump and probe beams with a dichroic mirror and tightly focus the beams to the sample plane using a 50× microscope objective lens (NA: 0.67); both beams are linearly polarized. We minimized and overlapped the pump and the probe beam foci in the sample plane by iterative (de)collimation and beam profiling, resulting in values of fwhm pump ∼0.6 μm (515 nm) and fwhm probe ∼0.7 μm (620 nm) and ∼0.82 μm (805 nm) at the same z position. The probe beam was passed through a galvo mirror system for scanning. A mechanical chopper modulates (chopping frequency f_{chop} = 4.37 kHz) the pump beam, and a variable delay line allows for acquiring pump−probe time-delay-dependent transient reflection measurements. A silicon photodiode and lock-in amplifier (Zurich Instruments MFLI) detects and demodulates the transient reflection signal, respectively.

Temperature-Dependent Permittivity Model. In order to model the permittivity ($\epsilon_{tot} = \epsilon'_{tot} + i\epsilon''_{tot}$) dynamics during the few picosecond stage where effective negative diffusion is observed, one can safely assume that the electron system has reached internal equilibrium (i.e., its distribution is described by Fermi−Dirac statistics), yet it is not at equilibrium with the lattice. Therefore, high temperature ellipsometry data (as obtained, e.g., in refs 54−56) is insufficient for our purposes, as it is obtained under steady-state conditions where $T_e = T_l$. Instead, since the differences between T_e and T_l are hard to measure, it is preferable to resort to a theoretical model. The permittivity model used in ref 30 accounted only for the contribution of intraband transitions to Au permittivity ($\epsilon_{Drude} = \epsilon'_{Drude} + i\epsilon''_{Drude}$). While this is suitable for the probe wavelength used in these studies (1.5 eV), the shorter probe wavelength used in the current work (2 eV) requires accounting also for the contribution of interband transitions to the permittivity (ϵ_{ib}, i.e., $\epsilon_{tot} = \epsilon_{Drude} + \epsilon_{ib}$). For brevity, we describe here only the latter.

Interband transitions (i.e., transitions between states in the d band and the s/p bands) occur in Au around either the L or X points in the band structure; see Figure 5a. They are

https://doi.org/10.1021/acsphotonics.2c01916
ACS Photonics 2023, 10, 1150−1158

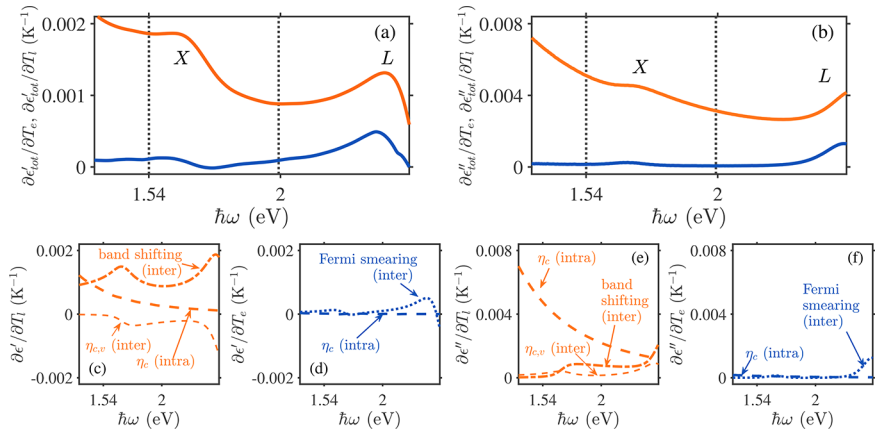

Figure 6. Sensitivity of (a) ϵ'_{tot} and (b) ϵ''_{tot} to T_e (blue solid lines) and to T_l (orange solid lines). (c,d) Dominant mechanisms responsible for the change of ϵ'_{Drude} or ϵ'_{ib} with T_l and T_e, respectively. (e,f) Same as (c,d) but for ϵ''_{Drude} or ϵ''_{ib}, respectively. In (c–f), the dotted, thick-dashed, thin-dashed, and dash-dotted lines represent the mechanisms of Fermi smearing, change of η_c contributing to the intraband transition, change of $\eta_{c,v}$ contributing to the interband transition, and band-shifting, respectively.

characterized by transition thresholds of ~2.3 and ~1.8 eV, respectively.[57]

The contributions of interband transitions to the permittivity are usually computed using the model developed by Rosei and co-workers.[57,59] This model is based on a standard calculation of $\Im(\epsilon_{ib}) = \epsilon''_{ib}$ via the population-weighted joint density of electron states and Fermi's golden rule, assuming thermal electron distributions and assuming the broadening of the individual electron energies is sufficiently small to be neglected. This parameter can be connected to the various electron collision mechanisms via the density matrix formulation (see refs 60–63). The different contributions to the permittivity predicted by this approach are listed in Figure 5b.

We note, however, that the broadening has a non-negligible dependence on the electron and phonon temperatures that disappears within the approach of refs 57 and 59. Thus, in order to test the importance of this additional sensitivity, we start with the so-called Lindhard-like model for the transverse permittivity of the material; by extending its frequency domain form (e.g., ref 64) to the time domain assuming the adiabatic approximation,[63,65] it becomes

$$\epsilon_{ib}(\omega; t) = 1 + \frac{2q_e^2}{\epsilon_0 m_e}\int d^3\mathbf{k}\frac{|\hat{\mathbf{e}}\cdot\mathbf{p}_{c,v}(\mathbf{k}, T_l(t))|^2}{(\mathcal{E}_c(\mathbf{k}) - \mathcal{E}_v(\mathbf{k}))^2/\hbar^2}\frac{f^T(\mathcal{E}_c(\mathbf{k}); T_e(t)) - f^T(\mathcal{E}_v(\mathbf{k}); T_e(t))}{\mathcal{E}_c(\mathbf{k}) - \mathcal{E}_v(\mathbf{k}) - \hbar\omega - i\hbar\eta_{c,v}(T_e(t), T_l(t), t)}$$

Here, q_e is the electron charge, ϵ_0 is the vacuum permittivity, m_e is the free electron mass, $\hat{\mathbf{e}}$ is the polarization vector and $\mathbf{p}_{c,v}$ is the matrix element of the electron momentum operator between states in the conduction and valence bands; its value at room temperature is taken from ref 66. $\eta_{c,v}(T_e(t), T_l(t), t) = (\eta_c(T_e(t), T_l(t), t) + \eta_v)/2$ is the average level broadening (namely, damping or collision rate) with the indices c and v signifying the final and the initial states in the absorption event. Specifically, $\eta_c = \eta_{c,e-e} + \eta_{c,e-ph}$ is the damping rate following Matthiessen's rule,[60] where $\eta_{c,e-e}$ and $\eta_{c,e-ph}$ are, respectively, the collision rates associated with the electron–electron and electron–phonon interactions.[60,67] These temperature- and time-dependent rates are calculated by taking the functional derivative of the corresponding interaction terms with respect to the electron distribution.[25,61] $\eta_v = 0.1$ fs^{-1}[68] is the collision rate associated with the electrons in the d-band; it is assumed to be time-independent since the electron distribution in the d-band remains nearly unchanged over time. This is due to the high density of states of the d-band. $\mathcal{E}_{c/v}$ is the energy of the electron in the conduction/valence band state $|\psi_{c/v}\rangle$ of the studied metal nanostructure whose occupation is given by the Fermi–Dirac distribution $f^T(\mathcal{E}_{c/v}; T_e(t))$. The electron distribution dynamics $f^T(\mathcal{E}_{c/v}; T_e(t))$ that follow the sub-picosecond-scale thermalization is dominated by the electron–phonon interactions, which are much slower than the damping rate. Thus, the permittivity can be assumed to change with the electron distribution adiabatically so that the time variable appearing here is associated with the probe envelope (see more details in ref 63). Moreover, we neglect the T_e dependence of the chemical potential because T_e is much smaller than the Fermi temperature.[60]

Figure 6a,b shows the derivatives of the metal permittivity with respect to the electron and phonon temperatures via the mechanism of Fermi smearing, change of η_c, and band-shifting (see their individual effects in Figure 6c,d). The Fermi smearing mechanism refers to the change in Fermi distribution with T_e. The band shifting is a consequence of the lattice expansion with increasing T_l, resulting in a change of the transition matrix element $\mathbf{p}_{c,v}$ and transition threshold for X and L transitions.[57,69–71] One can appreciate that while the sensitivity of the permittivity to T_l is always greater than the sensitivity to T_e, the *relative* importance of the latter is much higher at the shorter probe wavelength used (2 eV) compared to the longer wavelength originally used in ref 30 (1.54 eV). This happens because of the greater sensitivity of the contribution of interband transitions to T_e due to Fermi smearing (dotted blue lines in Figure 6c–f), the weaker dependence of the intraband contribution due to the dependence of η_c on T_l (thick dashed orange line) and the negative contribution of $\eta_{c,v}$ due to interband transitions (thin dashed orange line). The latter effect is particularly strong close to the L point and is the main novelty in the model used in this work. The additional effects we modeled (effect of Fermi smearing on the contribution of intraband transitions and the temperature dependence of the broadening η_c) were found to be relatively small (hence, negligible).

https://doi.org/10.1021/acsphotonics.2c01916
ACS Photonics 2023, 10, 1150–1158

AUTHOR INFORMATION

Corresponding Author

Yonatan Sivan − *School of Electrical and Computer Engineering, Ben-Gurion University of the Negev, Be'er Sheva 8410501, Israel;* orcid.org/0000-0003-4361-4179; Email: sivanyon@bgu.ac.il

Authors

Alexander Block − *Catalan Institute of Nanoscience and Nanotechnology (ICN2), BIST and CSIC, 08193 Bellaterra, Spain;* orcid.org/0000-0001-9288-5405

Renwen Yu − *Department of Electrical Engineering, Ginzton Laboratory, Stanford University, Stanford, California 94305, United States;* orcid.org/0000-0002-9701-5270

Ieng-Wai Un − *School of Electrical and Computer Engineering, Ben-Gurion University of the Negev, Be'er Sheva 8410501, Israel;* orcid.org/0000-0002-7156-0019

Sebin Varghese − *Catalan Institute of Nanoscience and Nanotechnology (ICN2), BIST and CSIC, 08193 Bellaterra, Spain;* orcid.org/0000-0001-7204-7121

Matz Liebel − *ICFO-Institut de Ciencies Fotoniques, The Barcelona Institute of Science and Technology, 08860 Castelldefels, Spain*

Niek F. van Hulst − *ICFO-Institut de Ciencies Fotoniques, The Barcelona Institute of Science and Technology, 08860 Castelldefels, Spain; ICREA-Institució Catalana de Recerca i Estudis Avançats, 08010 Barcelona, Spain;* orcid.org/0000-0003-4630-1776

Shanhui Fan − *Department of Electrical Engineering, Ginzton Laboratory, Stanford University, Stanford, California 94305, United States;* orcid.org/0000-0002-0081-9732

Klaas-Jan Tielrooij − *Catalan Institute of Nanoscience and Nanotechnology (ICN2), BIST and CSIC, 08193 Bellaterra, Spain; Department of Applied Physics, TU Eindhoven, 5612 AZ Eindhoven, The Netherlands;* orcid.org/0000-0002-0055-6231

Complete contact information is available at: https://pubs.acs.org/10.1021/acsphotonics.2c01916

Author Contributions

¶A.B., R.Y., and I.-W.U. contributed equally to this work.

Funding

ICN2 was supported by the Severo Ochoa program from Spanish MINECO Grant No. SEV-2017-0706. K.J.T. acknowledges funding from the European Union's Horizon 2020 research and innovation program under Grant Nos. 804349 (ERC StG CUHL) and 101069363 (ERC PoC COOLGRAELE), RYC fellowship No. RYC-2017-22330, and IAE project PID2019-111673GB-I00. M.L. and N.F.v.H. acknowledge support through the RTI2018-099957-J-I00 and PID2021-123814OB-I00 projects funded by MCIN/AEI/10.13039/501100011033/FEDER. ICFO was supported by Spanish MCIN Severo Ochoa program (CEX2019-000910-S), Fundació Privada Cellex, Fundació Privada Mir-Puig, and Generalitat de Catalunya through the CERCA program. I.W. and Y.S. were supported by Israel Science Foundation (ISF) grant (340/2020). S.F. acknowledges the support by a MURI program from the U.S. Army Research Office (Grant No. W911NF-19-1-0279).

Notes

The authors declare no competing financial interest.

REFERENCES

(1) Baffou, G.; Cichos, F.; Quidant, R. Applications and challenges of thermoplasmonics. *Nat. Mater.* **2020**, *19*, 946−958.
(2) Yu, R.; García de Abajo, F. J. Electrical Detection of Single Graphene Plasmons. *ACS Nano* **2016**, *10*, 8045−8053.
(3) Guo, Q.; Yu, R.; Li, C.; Yuan, S.; Deng, B.; García de Abajo, F. J.; Xia, F. Efficient Electrical Detection of Mid-Infrared Graphene Plasmons at Room Temperature. *Nat. Mater.* **2018**, *17*, 986−992.
(4) Yuan, S.; Yu, R.; Ma, C.; Deng, B.; Guo, Q.; Chen, X.; Li, C.; Chen, C.; Watanabe, K.; Taniguchi, T.; García de Abajo, F. J.; Xia, F. Room Temperature Graphene Mid-Infrared Bolometer with a Broad Operational Wavelength Range. *ACS Photonics* **2020**, *7*, 1206−1215.
(5) Lee, Y. K.; Jung, C. H.; Park, J.; Seo, H.; Somorjai, G. A.; Park, J. Y. Surface Plasmon-Driven Hot Electron Flow Probed with Metal-Semiconductor Nanodiodes. *Nano Lett.* **2011**, *11*, 4251−4255.
(6) Atar, F. B.; Battal, E.; Aygun, L. E.; Daglar, B.; Bayindir, M.; Okyay, A. K. Plasmonically enhanced hot electron based photovoltaic device. *Opt. Express* **2013**, *21*, 7196−7201.
(7) Boyer, D.; Tamarat, P.; Maali, A.; Lounis, B.; Orrit, M. Photothermal imaging of nanometer-sized metal particles among scatterers. *Science* **2002**, *297*, 1160−1163.
(8) Berciaud, S.; Lasne, D.; Blab, G. A.; Cognet, L.; Lounis, B. Photothermal heterodyne imaging of individual metallic nanoparticles: Theory versus experiment. *Phys. Rev. B* **2006**, *73*, 045424.
(9) Wang, L.; Li, B. Thermal memory: A storage of phononic information. *Phys. Rev. Lett.* **2008**, *101*, 267203.
(10) Greffet, J.-J.; Bouchon, P.; Brucoli, G.; Marquier, F. Light Emission by Nonequilibrium Bodies: Local Kirchhoff Law. *Phys. Rev. X* **2018**, *8*, 021008.
(11) Yu, R.; Guo, Q.; Xia, F.; García de Abajo, F. J. Photothermal engineering of graphene plasmons. *Phys. Rev. Lett.* **2018**, *121*, 057404.
(12) Baffou, G.; Bordacchini, I.; Baldi, A.; Quidant, R. Simple Experimental Procedures to Discern Photothermal Processes in Plasmon-Driven Chemistry. *Light: Sci. Appl.* **2020**, *9*, 108.
(13) Sivan, Y.; Dubi, Y. Recent Developments in Plasmon-Assisted Photocatalysis - a Personal Perspective. *Appl. Phys. Lett.* **2020**, *117*, 130501.
(14) Jain, P. K. Taking the Heat Off of Plasmonic Chemistry. *J. Phys. Chem. C* **2019**, *123*, 24347−24351.
(15) Wang, Z.; Zhang, K.; Zhang, B.; Tong, Z.; Mao, S.; Bai, H.; Lu, Y. Ultrafast battery heat dissipation enabled by highly ordered and interconnected hexagonal boron nitride thermal conductive composites. *Green Energy and Environment* **2022**, *7*, 1401−1410.
(16) Downer, M.; Shank, C. Ultrafast heating of silicon on sapphire by femtosecond optical pulses. *Phys. Rev. Lett.* **1986**, *56*, 761.
(17) Ostler, T.; Barker, J.; Evans, R.; Chantrell, R.; Atxitia, U.; Chubykalo-Fesenko, O.; El Moussaoui, S.; Le Guyader, L.; Mengotti, E.; Heyderman, L.; et al. Ultrafast heating as a sufficient stimulus for magnetization reversal in a ferrimagnet. *Nat. Commun.* **2012**, *3*, 666.
(18) Yu, R.; Alaee, R.; Boyd, R. W.; de Abajo, F. J. G. Ultrafast topological engineering in metamaterials. *Phys. Rev. Lett.* **2020**, *125*, 037403.
(19) Sivan, Y.; Ctistis, G.; Yüce, E.; Mosk, A. Femtosecond-scale switching based on excited free-carriers. *Opt. Exp.* **2015**, *23*, 16416−16428.
(20) Stoll, T.; Maioli, P.; Crut, A.; Del Fatti, N.; Vallee, F. Advances in femto-nano-optics: ultrafast nonlinearity of metal nanoparticles. *Eur. Phys. J. B* **2014**, *87*, 260.
(21) Groeneveld, R. H. M.; Sprik, R.; Lagendijk, A. Femtosecond spectroscopy of electron-electron and electron-phonon energy relaxation in Ag and Au. *Phys. Rev. B* **1995**, *51*, 11433−11445.
(22) Pelton, M.; Sader, J. E.; Burgin, J.; Liu, M.; Guyot-Sionnest, P.; Gosztola, D. Damping of acoustic vibrations in gold nanoparticles. *Nature Nanotechnol.* **2009**, *4*, 492.
(23) O'Brien, K.; Lanzillotti-Kimura, N.; Rho, J.; Suchowski, H.; Yin, X.; Zhang, X. Ultrafast acousto-plasmonic control and sensing in complex nanostructures. *Nat. Commun.* **2014**, *5*, 4042.

(24) Crut, A.; Maioli, P.; Del Fatti, N.; Vallee, F. Time-domain investigation of the acoustic vibrations of metal nanoparticles: Size and encapsulation effects. *Ultrasonics* **2015**, *56*, 98−108.
(25) Sarkar, S.; Un, I. W.; Sivan, Y. The electronic and thermal response of low electron density Drude materials to ultrafast optical illumination. *Phys. Rev. Applied* **2023**, *19*, 014005.
(26) Massicotte, M.; Soavi, G.; Principi, A.; Tielrooij, K.-J. Hot carriers in graphene − fundamentals and applications. *Nanoscale* **2021**, *13*, 8376−8411.
(27) Emiliani, V.; Guenther, T.; Lienau, C.; Nötzel, R.; Ploog, K. Femtosecond near-field spectroscopy: carrier relaxation and transport in single quantum wires. *J. Microsc.* **2001**, *202*, 229−240.
(28) Najafi, E.; Ivanov, V.; Zewail, A.; Bernardi, M. Super-diffusion of excited carriers in semiconductors. *Nat. Commun.* **2017**, *8*, 15177.
(29) Gaffney, K.; Chapman, H. N. Imaging atomic structure and dynamics with ultrafast X-ray scattering. *Science* **2007**, *316*, 1444−1448.
(30) Block, A.; Liebel, M.; Yu, R.; Spector, R.; Sivan, Y.; García de Abajo, F. J.; van Hulst, N. F. Tracking ultrafast hot-electron diffusion in space and time by ultrafast thermomodulation microscopy. *Sci. Adv.* **2019**, *5*, No. eaav8965.
(31) Segovia, M.; Xu, X. High Accuracy Ultrafast Spatiotemporal Pump−Probe Measurement of Electrical Thermal Transport in Thin Film Gold. *Nano Lett.* **2021**, *21*, 7228−7235.
(32) Guo, Z.; Manser, J. S.; Wan, Y.; Kamat, P. V.; Huang, L. Spatial and temporal imaging of long-range charge transport in perovskite thin films by ultrafast microscopy. *Nat. Commun.* **2015**, *6*, 7471.
(33) Block, A.; Principi, A.; Hesp, N. C.; Cummings, A. W.; Liebel, M.; Watanabe, K.; Taniguchi, T.; Roche, S.; Koppens, F. H.; van Hulst, N. F.; et al. Observation of giant and tunable thermal diffusivity of a Dirac fluid at room temperature. *Nat. Nanotechnol.* **2021**, *16*, 1195−1200.
(34) Sivan, Y.; Spector, M. Ultrafast dynamics of optically heat gratings in metals. *ACS Photonics* **2020**, *7*, 1271−1279.
(35) Spector, M.; Derevyanko, S. Controlling surface plasmon polariton losses in the visible spectrum by temperature-induced interband transitions. *Phys. Rev. B* **2022**, *106*, 125111.
(36) Vatsya, S. R.; Virk, K. S. Solution of two-temperature thermal diffusion model of laser−metal interactions. *Journal of Laser Applications* **2003**, *15*, 273.
(37) Huang, J.; Zhang, Y.; Chen, J. Ultrafast solid−liquid−vapor phase change in a thin gold film irradiated by multiple femtosecond laser pulses. *Int. J. Heat Mass Transfer* **2009**, *52*, 3091−3100.
(38) Maznev, A. A.; Johnson, J. A.; Nelson, K. A. Non-equilibrium transient thermal grating relaxation in metal. *Appl. Phys.* **2011**, *109*, 073517.
(39) Ren, Y.; Chen, J. K.; Zhang, Y. Optical properties and thermal response of copper films induced by ultrashort-pulsed lasers. *J. Appl. Phys.* **2011**, *110*, 113102.
(40) Al-Malkawi, G. H.; Hassanein, A. Impact of the electron-phonon coupling factor and electron heat capacity on the thermal response of targets irradiated by femtosecond laser. *Journal of Laser Applications* **2018**, *30*, 042004.
(41) Rosati, R.; Perea-Causin, R.; Brem, S.; Malic, E. Negative effective excitonic diffusion in monolayer transition metal dichalcogenides. *Nanoscale* **2020**, *12*, 356−363.
(42) Berghuis, A. M.; Raziman, T. V.; Halpin, A.; Wang, S.; Curto, A. G.; Rivas, J. G. Effective Negative Diffusion of Singlet Excitons in Organic Semiconductors. *Phys. Chem. Lett.* **2021**, *12*, 1360−1366.
(43) Anisimov, S.; Kapeliovich, B.; Perelman, T. Electron emission from metal surfaces exposed to ultrashort laser pulses. *Zh. Eksp. Teor. Fiz* **1974**, *66*, 375−377.
(44) Rethfeld, B.; Ivanov, D. S.; Garcia, M. E.; Anisimov, S. I. Modelling ultrafast laser ablation. *J. Phys. D: Appl. Phys.* **2017**, *50*, 193001.
(45) Hopkins, P. E. Contributions of Inter and Intra-band Excitations to Electron Heat Capacity and Electron-Phonon Coupling in Noble Metals. *J. Heat Transfer* **2010**, *132*, 014504.
(46) Vallée, F.; Fatti, N. D. Ultrafast Nonlinear Plasmonics. In *Plasmonics: Theory and Applications*; Shahbazyan, T. V., Stockman, M. I., Eds.; Springer, 2010.
(47) Brown, A. M.; Sundararaman, R.; Narang, P.; Goddard, W. A.; Atwater, H. A. Ab initio phonon coupling and optical response of hot electrons in plasmonic metals. *Phys. Rev. B* **2016**, *94*, 075120.
(48) Block, A. Quantifying nanoscale carrier diffusion with ultrafast optical and photocurrent microscopy. PhD Thesis, ICFO-Institut de Ciencies Fotoniques, 2019.
(49) Del Fatti, N.; Voisin, C.; Achermann, M.; Tzortzakis, S.; Christofilos, D.; Vallee, F. Nonequilibrium electron dynamics in noble metals. *Phys. Rev. B* **2000**, *61*, 16956−16966.
(50) Masia, F.; Langbein, W.; Borri, P. Measurement of the dynamics of Plasmons inside individual gold nanoparticles Using a femtosecond phase-resolved microscope. *Phys. Rev. B* **2012**, *85*, 235403.
(51) Dias, E. J. C.; Yu, R.; García de Abajo, F. J. Thermal Manipulation of Plasmons in Atomically Thin Films. *Light Sci. Appl.* **2020**, *9*, 87.
(52) Gao, G.; Jiang, L.; Xue, B.; Yang, F.; Wang, T.; Wan, Y.; Zhu, T. Unconventional Shrinkage of Hot Electron Distribution in Metal Directly Visualized by Ultrafast Imaging. *Small Methods* **2023**, *7*, 2201260.
(53) Varghese, S.; Mehew, J. D.; Block, A.; Reig, D. S.; Wozniak, P.ł; Farris, R.; Zanolli, Z.; Ordejon, P.; Verstraete, M. J.; van Hulst, N. F.; Tielrooij, K.-J. A pre-time-zero spatiotemporal microscopy technique for the ultrasensitive determination of the thermal diffusivity of thin films. *Rev. Sci. Instrum* **2023**, *94*, 034903.
(54) Reddy, H.; Guler, U.; Kildishev, A. V.; Boltasseva, A.; Shalaev, V. M. Temperature-dependent optical properties of gold thin films. *Optical Materials Express* **2016**, *6*, 2776−2802.
(55) Shen, P.-T.; Sivan, Y.; Lin, C.-W.; Liu, H.-L.; Chang, C.-W.; Chu, S.-W. Temperature- and -roughness dependent permittivity of annealed/unannealed gold films. *Opt. Exp.* **2016**, *24*, 19254.
(56) Magnozzi, M.; Ferrera, M.; Mattera, L.; Canepa, M.; Bisio, F. Plasmonics of Au nanoparticles in a hot thermodynamic bath. *Nanoscale* **2019**, *11*, 1140−1146.
(57) Guerrisi, M.; Rosei, R.; Winsemius, P. Splitting of the interband absorption edge in Au. *Phys. Rev. B* **1975**, *12*, 557−563.
(58) Rangel, T.; Kecik, D.; Trevisanutto, P. E.; Rignanese, G.-M.; Van Swygenhoven, H.; Olevano, V. Band structure of gold from many-body perturbation theory. *Phys. Rev. B* **2012**, *86*, 125125.
(59) Rosei, R. Temperature modulation of the optical transitions involving the Fermi surface in Ag: Theory. *Phys. Rev. B* **1974**, *10*, 474−483.
(60) Ashcroft, N. W.; Mermin, N. D. *Solid State Physics*; Brooks/Cole, 1976.
(61) Coleman, P. *Introduction to Many Body Physics*; Cambridge University Press, 2015.
(62) Bruus, H.; Flensberg, K. *Many-Body Quantum Theory in Condensed Matter Physics: An Introduction*; OUP: Oxford, 2004.
(63) Un, I. W.; Sarkar, S.; Sivan, Y. An electronic-based model of the optical nonlinearity of low electron density Drude materials. *Phys. Rev. Applied* **2023**, *19*, 014005.
(64) Grosso, G.; Parravicini, G. *Solid State Physics*, 2nd ed.; Academic Press: London, 2014.
(65) Saavedra, J. R. M.; Asenjo-Garcia, A.; Garcia de Abajo, F. J. Hot-Electron Dynamics and Thermalization in Small Metallic Nanoparticles. *ACS Photonics* **2016**, *3*, 1637−1646.
(66) Marini, A; Conforti, M; Della Valle, G; Lee, H W; Tran, T. X; Chang, W; Schmidt, M A; Longhi, S; St J Russell, P; Biancalana, F Ultrafast nonlinear dynamics of surface plasmon polaritons in gold nanowires due to the intrinsic nonlinearity of metals. *New. J. Phys.* **2013**, *15*, 013033.
(67) Snoke, D. W. *Solid State Physics: Essential Concepts*, 2nd ed.; Pearson/Addison-Wesley: Boston, MA, 2020.
(68) Marini, A.; Biancalana, F. Ultrashort Self-Induced Transparency Plasmon Solitons. *Phys. Rev. Lett.* **2013**, *110*, 243901.

https://doi.org/10.1021/acsphotonics.2c01916
ACS Photonics 2023, 10, 1150−1158

(69) Christensen, N.; Seraphin, B. Relativistic Band Calculation and the Optical Properties of Gold. *Phys. Rev. B* **1971**, *4*, 3321−3344.
(70) Winsemius, P.; van Kampen, F. F.; Lengkeek, H. P.; van Went, C. G. Temperature dependence of the optical properties of Au, Ag and Cu. *J. Phys. F: Met. Phys.* **1976**, *6*, 1583.
(71) Winsemius, P.; Guerrisi, M.; Rosei, R. Splitting of the interband absorption edge in Au:Temperature dependence. *Phys. Rev. B* **1975**, *12*, 4570−4572.

https://doi.org/10.1021/acsphotonics.2c01916
ACS Photonics 2023, 10, 1150−1158